remote sensing

MDPI

Article

First Retrieval of Sea Surface Currents Using L-Band SAR in Satellite Formation

Bo Pan [1], Xinzhe Yuan [2], Tao Li [3], Tao Lai [1,*], Xiaoqing Wang [1], Chengji Xu [4] and Haifeng Huang [1]

[1] School of Electronic and Communication Engineering, Sun Yat-sen University, Shenzhen 518107, China; panb6@mail2.sysu.edu.cn (B.P.); wangxq58@mail.sysu.edu.cn (X.W.); huanghaifeng@mail.sysu.edu.cn (H.H.)
[2] National Satellite Ocean Application Service, Beijing 100081, China; harley_yuan@mail.nsoas.org.cn
[3] Land Satellite Remote Sensing Application Center, Beijing 100048, China; rs_litao@163.com
[4] School of Systems Science and Engineering, Sun Yat-sen University, Guangzhou 510275, China; xuchj9@mail2.sysu.edu.cn
* Correspondence: lait3@mail.sysu.edu.cn

Abstract: The inversion of ocean currents is a significant challenge and area of interest in ocean remote sensing. Spaceborne along-track interferometric synthetic aperture radar (ATI-SAR) has several advantages and benefits, including precise observations, extensive swath coverage, and high resolution. However, a limited number of spaceborne interferometric synthetic aperture radar (InSAR) systems are operating in orbit. Among these, the along-track baseline length is generally suboptimal, resulting in low inversion accuracy and difficulty in achieving operational stability. One of the approaches involves employing lower-frequency bands such as the L band to increase the baseline length to achieve the optimal baseline for a satellite formation. The LuTan-1 mission, the world's first L-band distributed spaceborne InSAR system, was successfully launched on 27 February 2022. L-band distributed formation operation provides insight into the development of future spaceborne ATI systems with application to new exploration regimes and under optimal baseline conditions. There are two novel aspects of this investigation: (1) We described the ocean current inversion process and results based on LuTan-1 SAR data for the first time. (2) A cross-track baseline component phase removal method based on parameterized modeling was proposed for distributed InSAR systems. Both qualitative and quantitative comparisons validated the effectiveness and accuracy of the inversion results.

Keywords: along-track interferometry (ATI); LuTan-1; sea surface currents; synthetic aperture radar (SAR)

Academic Editor: Dusan Gleich

Received: 22 October 2024
Revised: 28 December 2024
Accepted: 30 December 2024
Published: 2 January 2025

Citation: Pan, B.; Yuan, X.; Li, T.; Lai, T.; Wang, X.; Xu, C.; Huang, H. First Retrieval of Sea Surface Currents Using L-Band SAR in Satellite Formation. *Remote Sens.* **2025**, *17*, 131. https://doi.org/10.3390/rs17010131

1. Introduction

Ocean currents [1], which are the persistent and directional movements of seawater, are subject to various influences, including wind, temperature fluctuations, salinity gradients, and the Earth's rotation [2]. They are an essential parameter in the dynamic environment of oceans and are indispensable for navigation, climate regulation, marine disaster forecasting, and the distribution of marine life [3]. The accurate measurement of ocean currents poses a significant challenge for scientific investigation and practical applications.

Spaceborne synthetic aperture radar (SAR) plays a vital role owing to its all-day, all-weather capability, wide field of view, and high spatial resolution. Ocean current inversion methods based on SAR can be broadly classified into two categories [4,5]: Doppler centroid analysis (DCA) and along-track interferometry (ATI). The DCA method applies to single-antenna SAR data. It imposes lower system requirements but yields relatively low

spatial resolution. Moreover, it generates one-dimensional velocity fields along the range direction. Contrarily, ATI requires SAR data from at least two antennas to generate interferograms, which involves higher system complexity. However, this approach facilitates higher accuracy and spatial resolution for current velocity and is less sensitive to antenna pointing errors.

ATI-SAR was initially proposed to detect ocean surface currents. The system sequentially monitors the same resolution cell on the ocean's surface by employing two antennas aligned along the flight direction. If the resolution cell contains motion along the radar line of sight, the distance between the second antenna and the resolution cell changes relative to the first antenna. This is manifested as a phase difference between the SAR complex images acquired by the two antennas, referred to as the interferometric phase [6]. Theoretically, the ocean current fields derived from ATI-SAR maintain the same high spatial resolution as SAR imagery [7]. This presents a significant advantage for studying sub-mesoscale oceanic phenomena like ship wakes.

The Shuttle Radar Topography Mission (SRTM) was the first experiment to employ spaceborne ATI-SAR for sea surface current inversion [8,9]. The mission utilised a deployable boom to establish a 7 m physical along-track baseline, which enabled an interferometric time delay of approximately 0.5 ms [10,11]. At a spatial resolution of 1 km, Romeiser et al. [12] successfully retrieved currents with an accuracy of approximately 0.2 m/s by processing the ATI data acquired by the X-SAR instrument over the Wadden Sea, the Netherlands. TerraSAR-X was the first spaceborne SAR system to implement ATI in divided antenna mode [6]. It supports two ATI configurations, a dual receive antenna (DRA) mode and an aperture switching (AS) mode, with a 1.15 m baseline length [13]. Romeiser was the first to process AS-mode data, obtaining a current measurement accuracy of 0.1 m/s at a 1 km spatial resolution [14]. In the same vein, Mamoon Rashid et al. [15,16] employed RADARSAT-2's dual-channel ATI mode to acquire a current measurement accuracy of 0.1 m/s at a spatial resolution of nearly 800 m over the Florida Current (FC) region, with an effective along-track baseline of 3.75 m. The ATI experimental mode is supported by Gaofen-3, which establishes a 3.75 m effective along-track baseline. For the first time, Yuan et al. [17] utilized this experimental mode to process data from the Jiaozhou Bays (located near Qingdao in Shandong Province, China). They reported a root-mean-square error (RMSE) of less than 0.2 m/s in comparison to high-frequency surface wave radar (HFSWR) data, resulting in an effective resolution of 1 km. Furthermore, the TerraSAR-X/TanDEM-X constellation is the very first distributed interferometric SAR system to accommodate the ATI mode, with an effective along-track baseline of 25 m [18,19]. Romeiser [20] conducted a comparison of the current measurements from the TerraSAR-X single-satellite DRA mode and the TerraSAR-X/TanDEM-X dual-satellite formation over the same oceanic region. The single-satellite DRA mode necessitated a spatial resolution of 1 km to achieve an accuracy of 0.1 m/s, whereas the dual-satellite formation with a long baseline enabled measurements at a resolution of 33 m. This enhancement is consistent with theoretical predictions that the optimal effective baseline length for X-band spaceborne ATI systems is between 20 and 30 m. Table 1 summarizes the preceding information.

One of the key challenges in achieving the operational implementation of spaceborne ATI-SAR is optimizing the baseline length, which directly impacts the accuracy of surface current measurements. Additionally, it is essential to maximize temporal coverage, defined as the proportion of time within a satellite's orbit during which the required measurement accuracy is maintained. ATI-SAR has strict requirements for baseline length. If the baseline is extremely short, the time delay between the two channels is also short, resulting in a phase that is easily overwhelmed by noise [20]. Conversely, the delay time between the two interfering channels will exceed the sea surface's coherence time, which occurs when

the surface scattering is stable. The coherence coefficient will be minimal, and consequently, it is impossible to obtain an effective interference phase.

Table 1. Spaceborne ATI platforms and their specifications.

Satellite Platform	Frequency Band	AT Baseline Length	Orbit Altitude	Accuracy @ Grid Size
SRTM [8–12]	X	7 m	∼233 km	0.2 m/s @ 1 km^2
TerraSAR-X [6,13,14]	X	1.15 m	∼514 km	0.1 m/s @ 1 km^2
RADARSAT-2 [15,16]	C	3.75 m	∼798 km	0.1 m/s @ 800 m^2
Gaofen-3 [17]	C	3.75 m	∼755 km	0.2 m/s @ 1 km^2
TerraSAR-X/TanDEM-X [18–20]	X	20∼30 m	∼514 km	0.1 m/s @ 33 m^2

The length of the optimal baseline has an approximately inverse relationship with the SAR frequency. There are two approaches for realizing optimal baseline operation for spaceborne ATI systems. The first is to use a solitary satellite. Given the hardware platform constraints, it is necessary to increase the SAR frequency band. For example, the Wavemill [21] and SEASTAR [22] satellite mission concepts, successively proposed by the European Space Agency (ESA), both consist of a satellite carrying a single Ku-band SAR payload. This instrument is based on the ATI solution with two squared-look directions to invert the ocean surface current vectors. The optimal baseline can be reduced by approximately 10 m owing to the higher band, which simplifies the satellite technology. Both studies conducted airborne proof-of-concept experiments and obtained encouraging results [23,24]. However, there are currently no thoroughly evaluated spaceborne platforms. Another approach is via satellite constellations. Roismer [25] demonstrated that for the TanDEM-X/TerraSAR-X constellations, the optimal X-band along-track effective baseline is 20–30 m. However, this baseline length is shorter than the minimum safe distance between satellites. Thus, the constellation can only operate within this optimal baseline for short periods, limiting temporal coverage. Contrarily, the optimal effective along-track baseline length for an L-band spaceborne ATI-SAR system is approximately 10 times that of a C-band system [26], reaching around 200–300 m. This significantly enhances the feasibility of using satellite constellations to achieve an optimal baseline. The actual temporal coverage depends on the specific satellite formation design, which is beyond the scope of this study.

The LuTan-1 constellation's A and B satellites (LT-1A/1B) were successfully launched from the Jiuquan Satellite Launch Center in China on 26 January and 27 February 2022, respectively [27]. LuTan-1 represents the world's first L-band distributed SAR dual-satellite system. This development also marked the first opportunity to invert ocean surface currents using the L-band spaceborne interferometric synthetic aperture radar (InSAR) technique. Compared to single-satellite systems, satellite formation systems employing longer baselines are prone to introducing larger errors. Owing to the limited precision of navigation systems and the irregular baseline variations induced by helical flight paths, baseline errors typically exhibit temporal variability. Therefore, it is challenging to remove the cross-track baseline phase component solely based on the satellite's onboard navigation system parameters. In response to the characteristics of LuTan-1 distributed InSAR system, this study proposes an easily implementable two-step strategy. The key aspect of this approach is the use of a parameterized model for baseline error correction, which provides a clear physical interpretation compared to the commonly used polynomial fitting methods. This model enables the complete removal of phase components induced by an across-track baseline, thereby facilitating high-accuracy ocean current inversion. For the first time, based on

LuTan-1, the inversion of sea surface currents was implemented in this study using the L-band satellite formation ATI technique, and its feasibility was evaluated.

The remainder of this report is organized as follows: Section 2 presents the fundamental principles of InSAR measurements. Section 3 provides an overview of the experimental datasets, including the LuTan-1 satellite data and the reference data. Sections 4 and 5 describe the data processing procedure and retrieved results, respectively. Finally, the main conclusions are summarized in Section 6.

2. Basic Principles

Employing a dual-antenna configuration, the LuTan-1 system acquires sea surface backscatter data, creating two complex images, and then processes them to obtain an interferogram image.

$$I = s_1(r_1)s_2^*(r_2) = |s_1(r_1)s_2(r_2)| \exp[j(\varphi_{A1} - \varphi_{A2})]. \quad (1)$$

where s denotes the complex SAR image data, φ is the phase, and r is the slant range from the SAR platform to the scatterer on the sea surface. The subscripts 1 and 2 correspond to the dual-receiver antenna configuration of the LuTan-1 SAR satellite system. The asterisk (*) indicates complex conjugation. Given that the LuTan-1 system operates as a hybrid baseline interferometric SAR system, the interferometric phase ϕ delineated in (1) comprises the along-track baseline component that is sensitive to velocity and the cross-track baseline component that is sensitive to the sea surface height. The hybrid baseline interferometric phase is expressed as follows:

$$\phi = \phi_{ATI} + \phi_{XTI} + \phi_{error} = \phi_d + \phi_h + \phi_{flat} + \phi_{error} \quad (2)$$

where ϕ_d represents the phase component induced by the ocean surface Doppler velocity, which is caused by the along-track baseline component; in addition to the contribution of the sea surface current velocity, this term also incorporates the effects of the Bragg phase velocity, the long-wave orbital velocity, etc. ϕ_{flat} and ϕ_h represent the flat Earth phase and topography phase, respectively, caused by the cross-track baseline components. ϕ_{error} contains all errors. To achieve velocity retrieval, the velocity-independent phase components should be removed.

2.1. ATI

Figure 1 illustrates the geometric configuration of an ideal ATI system. Two antennas, R_a and F_a, were mounted in line with the flight direction to sequentially image the sea surface current area within a certain time interval. The phase difference between the two complex images is proportional to the radial velocity of the sea-surface scatterers. Assume that at imaging time t, the distance between the sea-surface scatterer and the forward antenna F_a is R_1, and after a certain time interval Δt, the distance to the backward antenna R_a is R_2. During this interval, with the scatterers moving at a radial velocity V_r, the phase difference between F_a and R_a attributable to the sea surface scatterers can be calculated as follows:

$$\phi_{AT} = -\frac{4\pi}{\lambda}[R(t + \Delta t) - R(t)] = -\frac{4\pi}{\lambda} v_d \Delta t. \quad (3)$$

For a single-transmit dual-receiver system, such as LuTan-1, the effective baseline length was half the physical baseline length; therefore, the time delay $\Delta t = B_{AT}/2v_p$, where

B_{AT} is the physical baseline length and v_p is the platform velocity. Furthermore, the radial velocity of the sea surface scatterer can be obtained as follows:

$$v_d = \frac{\phi_{ATI}\lambda v_p}{2\pi B_{AT}}. \tag{4}$$

The one-dimensional component of the sea surface current along the ground range direction can be calculated as follows:

$$u_d = \frac{v_r}{\sin\theta}. \tag{5}$$

where θ denotes the incidence angle.

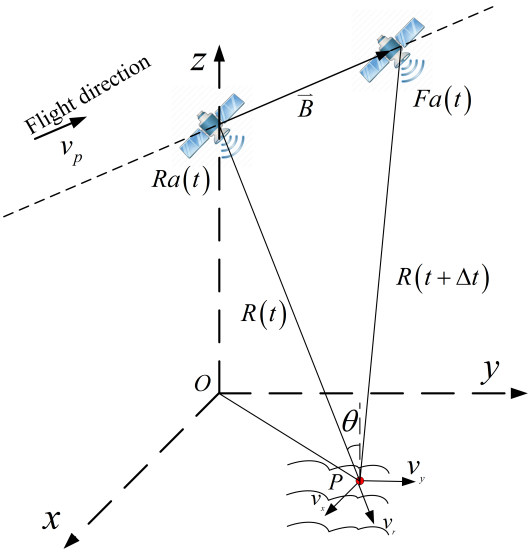

Figure 1. Schematic of along-track interferometry geometry.

2.2. Cross-Track Interferometry (XTI)

Figure 2 is a geometric schematic of the XTI. The sign $\otimes$ denotes the flight direction towards the paper. Antennas A_1 and A_2 are mounted perpendicularly to the flight path, and the angle between the baseline $\vec{B}$ and the horizontal direction is α. The two antennas image the same resolution unit of the sea surface simultaneously. Considering the slight difference in the imaging angles of the two antennas, the range difference of the radar echo signal is $\triangle R = R_1 - R_2$, where R_1 and R_2 are the distances from the two antennas to the sea surface scatterer P. The range difference can be transformed into an interference phase as follows:

$$\phi_{XT} = \frac{4\pi(R_2 - R_1)}{\lambda} = \frac{4\pi B_{XT}\sin(\theta - \alpha)}{\lambda} \tag{6}$$

where B_{XT} represents the length of the cross-track baseline, θ is the incidence angle, and α denotes the baseline inclination angle. After obtaining the interference phase ϕ_{XT}, the height of the target P relative to the reference plane h can be calculated based on the simple geometric relationship shown in Figure 2.

$$h = H - R_1\cos\left[\frac{\pi}{2} + \alpha - \arccos\left(-\frac{\lambda\phi_X}{4\pi B_{XT}}\right)\right]. \tag{7}$$

2.3. Sensitivity and Ambiguity

The SAR complex image can only record the main phase value within $[-\pi, \pi]$. When the phase difference caused by the sea surface velocity is greater than 2π, there is a difference of $2k\pi(k = \pm1, \pm2\ldots)$ between the recorded phase and the true phase value.

Substituting 2π into (4)–(7), the ambiguous velocity v_{amb} and ambiguous height h_{amb} can be calculated as (8) and (9), respectively:

$$v_{amb} = \frac{\lambda v_p}{B_{AT} \cdot \sin\theta}. \tag{8}$$

$$h_{amb} = \frac{\lambda}{2} \cdot \frac{r \cdot \sin\theta}{B_{XT}}. \tag{9}$$

For LuTan-1, v_{amb} = 5.8 m/s is obtained using Equation (8). This value exceeds the upper limit of the speed of most ocean currents worldwide. Regarding height ambiguity, h_{amb} is 45.64 m, which exceeds almost all sea surface heights worldwide. Therefore, it is likely that the experimental data will not produce velocity and height ambiguities.

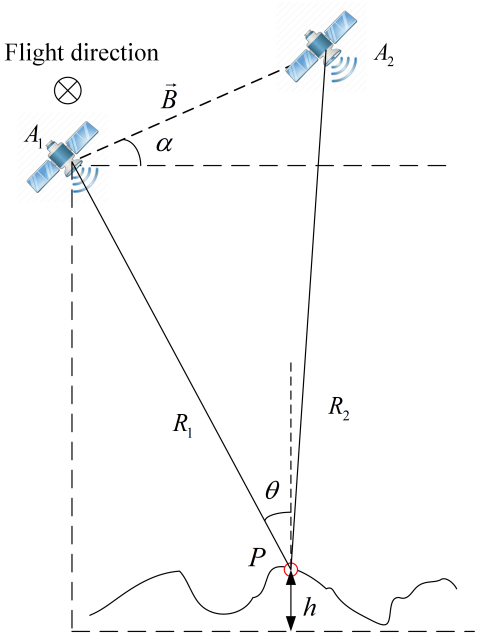

Figure 2. Schematic of across-track interferometry geometry.

3. LuTan-1 Interferometric Experiment

3.1. Satellite SAR Data and Test Area

LuTan-1 [28] is a high-resolution interferometric SAR mission that consists of twin satellites (A and B) carrying two SAR instruments operating at the L-band (f = 1.26 GHz) and orbiting in a double-helix formation [1]. The LuTan-1 data used here were acquired in the ascending pass, strip map, single transmission, and dual reception modes with the antenna looking to the right of the flight direction. Our dataset was acquired using HH polarization. The scene size for each acquisition was approximately 59 km in the azimuth direction and 55 km in the range direction, corresponding to an incidence angle varying between 27.86° and 32.28°. The pixel sizes in the azimuth and range directions were 1.40 m and 1.67 m, respectively. The projection of the hybrid baseline into the along-track direction was approximately 575 m (the effective base length was 287.5 m), corresponding to a delay time of approximately 39.49 ms. Considering the average wind speed of 4.6 m/s shown in Figure 5a, the coherence time [29] owing to the time-varying characteristics of the local sea surface was computed as 242.12 ms, which exceeded the delay time of LuTan-1. The main acquisition parameters for the investigated images are summarized in Table 2.

Table 2. LuTan-1 System Parameters.

Parameters	Parameter Values
Center Frequency	1.26 GHz
Platform Altitude	607 km
Band Width	80 MHz
Polarization Mode	HH
Orbit Orientation	Ascending
Center Incidence Angle (θ)	30°
Pulse Width	70 μs
Acquisition Date and Time (UTI)	18 July 2022 09:45:30
Antenna Operation Mode	Single transmission and dual reception

The interferometric images used in this study were obtained from the Yantai marine region of Shandong Peninsula, China, on 18 July 2022. The area covered by the satellite acquisition is shown in the red box in Figure 3. The Yantai Maritime Area consists of two main parts, the Bohai Sea and the northern Yellow Sea, connected by the Bohai Strait. The Bohai Sea region off Yantai, southeast of Bohai Bay, has an average water depth of 13 m and encompasses Laizhou Bay, Longkou Bay, and the mouths of seven major rivers. Intensity images of the primary (reference, serving as the benchmark) and secondary (aligned to the primary image for registration processing) images corresponding to the study area are shown in Figure 4.

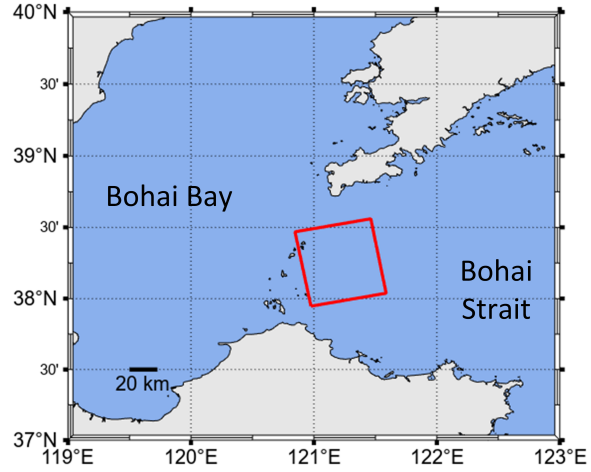

Figure 3. Geographical location of study area.

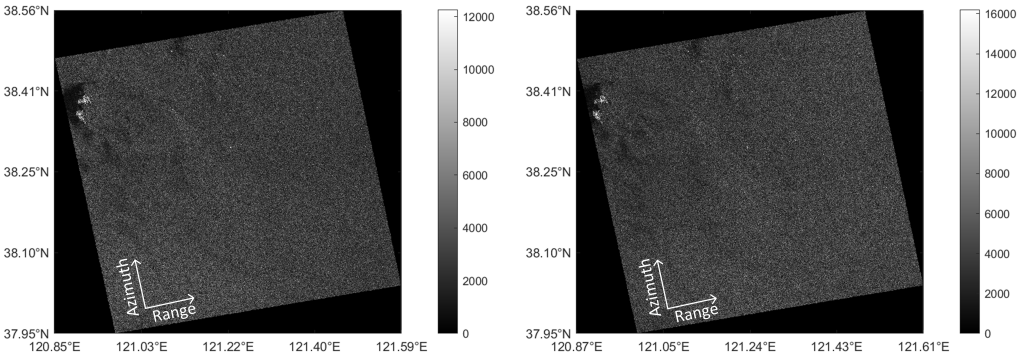

(**a**) (**b**)

Figure 4. (**a**) Intensity of primary image. (**b**) Intensity of secondary image.

3.2. Wind Field Data

Wind fields are the primary driving force of upper ocean dynamics and are closely linked to various oceanographic parameters, including sea surface current velocity. In this study, wind field data were obtained from the European Centre for Medium-Range Weather Forecasts (ECMWF) ERA5. This dataset represents the institution's fifth-generation reanalysis, providing comprehensive global wind speed data. We extracted the due-east u10 and due-north wind field components at a height of 10 m above the study sea area [30]. The ERA5 dataset used in this study had a temporal resolution of 1 h and a spatial resolution of 0.25° Lat/Lon. Figure 5a shows the wind field data corresponding to the study region.

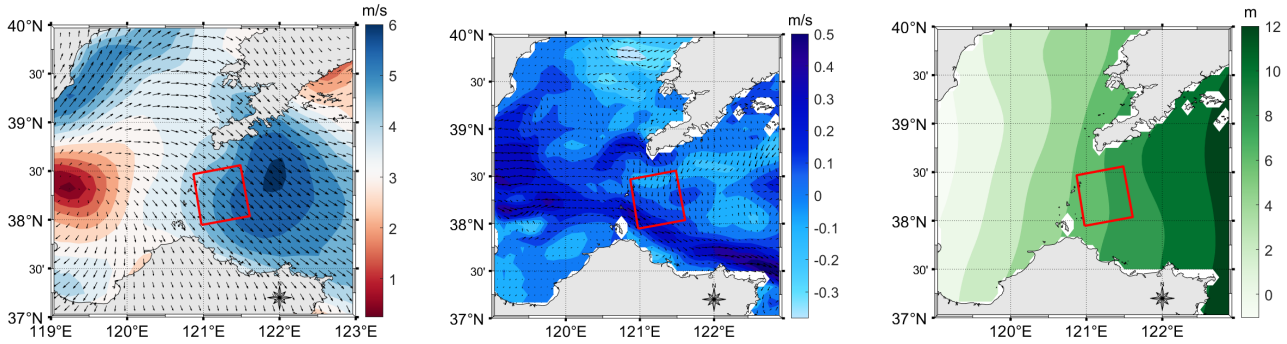

(**a**) (**b**) (**c**)

Figure 5. Reference data. (**a**) ECMWF wind field at 10 m height above sea surface. (**b**) CMEMS sea surface velocity. (**c**) CMEMS sea surface height.

3.3. Reference Data and Sea Surface Height Data

Owing to the hybrid baseline configuration of LuTan-1, it is sensitive to both sea surface velocity and sea surface height. To obtain accurate sea surface velocity, the sea surface height component should first be removed, and the derived velocity inversion results should then be compared to reference data. In this study, both the sea surface velocity and height reference data were sourced from the Copernicus Marine Environment Monitoring Service (CMEMS), with the product ID being "GLOBAL_ANALYSISFORECAST_PHY_007_022" [31]. The spatial resolution of the CMEMS data is 1/12° Lat/Lon, with a temporal resolution of 6 h. For sea surface velocity, CMEMS provides the velocity components in the true north and true east directions, which should be transformed into the radar line-of-sight direction to validate the current velocity results derived from LuTan-1. Regarding the sea surface height, the CMEMS provides data that are referenced to the Earth Gravitational Model 1996 (EGM96) geoid. The EGM96 geoid-based heights should be corrected by adding the geoid height anomaly to convert them into World Geodetic System 1984 (WGS84) ellipsoid-referenced heights. The reference sea surface height and velocity data from CMEMS are shown in Figure 5b,c, respectively. Note that there are significant differences in both temporal (hours vs. milliseconds) and spatial resolution (kilometers vs. meters) between the CMEMS data and the results obtained from LuTan-1. These discrepancies hinder complete agreement between the absolute measurements of the inversion results and reference data.

4. Data Processing

LuTan-1 is currently the only spaceborne InSAR system operating in the L-band. The configuration of the satellite formation enables optimal baseline operation over a wide temporal range. It should be noted that temporal coverage is closely related to the specific formation design, which is beyond the scope of this study. To the best of our knowledge, there are no studies that have employed LuTan-1 data for ocean current

inversion. This study presents, for the first time, a comprehensive workflow for sea surface current inversion using LuTan-1 data. The primary steps include image registration, random phase noise suppression (multi-look processing), and removal of the cross-track phase components. Owing to the limitations in satellite navigation accuracy, distributed systems exhibit more significant orbital errors compared to single-satellite systems. In interferometric processing, this manifests primarily as baseline errors, which exacerbates the difficulty of removing the flat Earth phase and height phase . To address this issue, we propose a parameter model-based approach for residual flat Earth and height phase removal. The overall workflow for ocean current inversion using LuTan-1 data is illustrated in Figure 6. Two SAR images acquired by the distributed satellite system are co-registered to obtain a coherence map and an interferometric phase map, following the method detailed in Section 4.1. Utilizing the metadata from the satellite system, including satellite ephemeris data and local sea surface height information, the slant range difference between the two satellites for the same sea surface target is calculated. This allows the theoretical flat Earth phase to be derived. The interferometric phase is then corrected by subtracting this theoretical flat Earth phase, resulting in the residual phase denoted as ϕ_1. The residual phase ϕ_1 undergoes phase filtering and phase unwrapping processes. Subsequently, it is fitted using a weighted least-squares approach, as described in Equation (19), where the weighting coefficients correspond to the coherence values. The fitted phase is then subtracted from ϕ_1, yielding the fully flattened phase. Finally, after geocoding, the flattened phase is converted into the sea surface velocity.

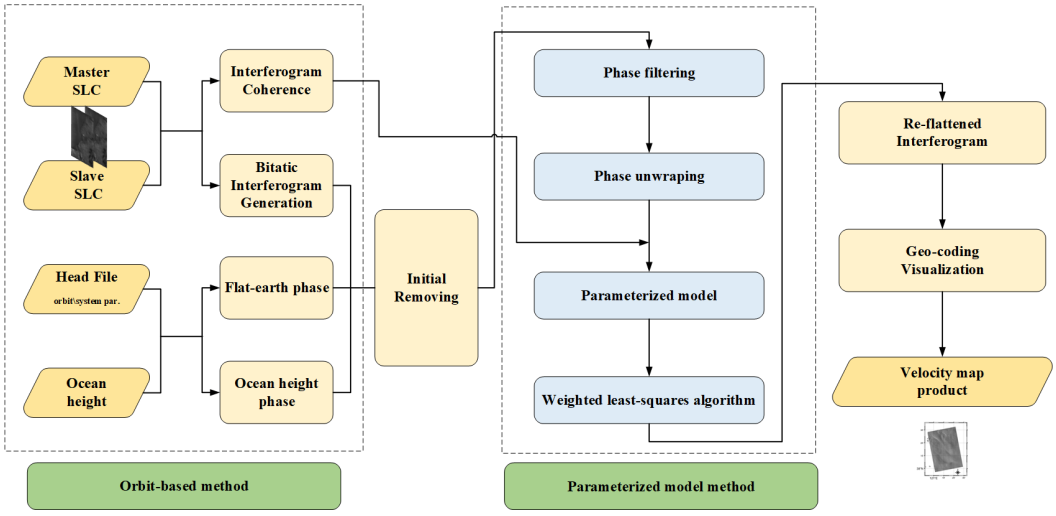

Figure 6. Flowchart of surface current extraction processor for distributed SAR interferometry.

4.1. Image Registration

The interference phase's quality is the primary determinant of velocity precision. Obtaining a high-quality interference phase requires high-precision registration of complicated pictures. For interferometric data processing, complicated image registration is therefore essential. As per the various metric functions employed, the registration techniques may be broadly classified into three categories: the correlation function method, the average fluctuation method, and the maximum spectrum method [32]. The correlation function approach is now the most popular among them because of its strong stability and excellent effectiveness [33]. For interferometric data processing, the correlation function approach is used as the registration procedure in the two global interference mapping projects, TanDEM-X and SRTM [34]. The correlation function can be classified as either real or complex correlation [35]. The complex correlation function's registration accuracy is

superior to the actual correlation function in regions with strong coherence and comparatively consistent scattering properties, such the sea surface, according to studies [34]. A complex correlation function was used as the metric function in this investigation. The complex correlation coefficient can be expressed using Equation (10).

$$\gamma(u,v) = \frac{\left|\sum_{m=0}^{M-1}\sum_{n=0}^{N-1} u_1(m,n)u_2(m+u,n+v)^*\right|}{\sqrt{\sum_{m=0}^{M-1}\sum_{n=0}^{N-1}|u_1(m,n)|^2}\sqrt{\sum_{m=0}^{M-1}\sum_{n=0}^{N-1}|u_2(m+u,n+v)|^2}} \tag{10}$$

Here, μ_1 and μ_2 denote the two SAR Single Look Complex (SLC) images, while M and N symbolize the size of the window used for computation. (u,v) denotes the sliding position of the correlation calculations, and (m,n) denotes the pixel position in the SAR image. The symbol $|\ \ |$ indicates the absolute value of the conjugate operation. The Fourier transformation of the cross-correlation function of the two images equals the product of the Fourier transformation of one image and the conjugate of the Fourier transformation of the other. Therefore, the correlation functions in (10) can be implemented using Fast Fourier Transform (FFT) to enhance computational efficiency, as shown in Equation (11).

$$\begin{aligned}\gamma = \mathrm{norm}(|\ & IFFT(FFT(u_1(m,n)) \\ & FFT(u_2(m,n))^*)\ |)\end{aligned} \tag{11}$$

Here, norm( ) represents the normalization operation. The term FFT stands for Fast Fourier Transform, and $IFFT$ represents inverse Fast Fourier Transform. For SAR interferometric images, the registration precision should generally be better than 1/8 of the pixel. Sub-pixel-level displacement can be estimated through interpolation.

The final step involves adjusting the secondary image based on the calculated offsets, as described in (12). Here, S and s represent the secondary images before and after registration, respectively, δ_A signifies the offset of the block in the azimuth direction, and δ_R refers to the offset of the block in the range direction. Additionally, size A and size R represent the block lengths in the azimuth and range directions, respectively.

$$S = \mathrm{IFFT}\left(FFT(s)\cdot\exp\left(-2\pi j\left(\frac{\delta_A}{\text{size } A}+\frac{\delta_R}{\text{size } R}\right)\right)\right). \tag{12}$$

Figure 7a shows the correlation coefficients between the primary image and the secondary image of LuTan-1 after registration. The figure illustrates a correlation coefficient ranging from 0.4 to 0.95. The central portion of the image has a larger correlation coefficient because of its comparatively elevated signal-to-noise ratio. These results suggest a strong correlation between primary and secondary images after registration. To enhance the clarity of the presentation, given the large scene scale and the high fringe density, the interferometric phase diagram (Figure 7b) is limited to the region outlined by the red box in Figure 7a. The interference fringe patterns in other regions of the image exhibit analogous interferometric patterns. The figure shows that the interferometric fringes are clear and sharp, indicating a good registration effect.

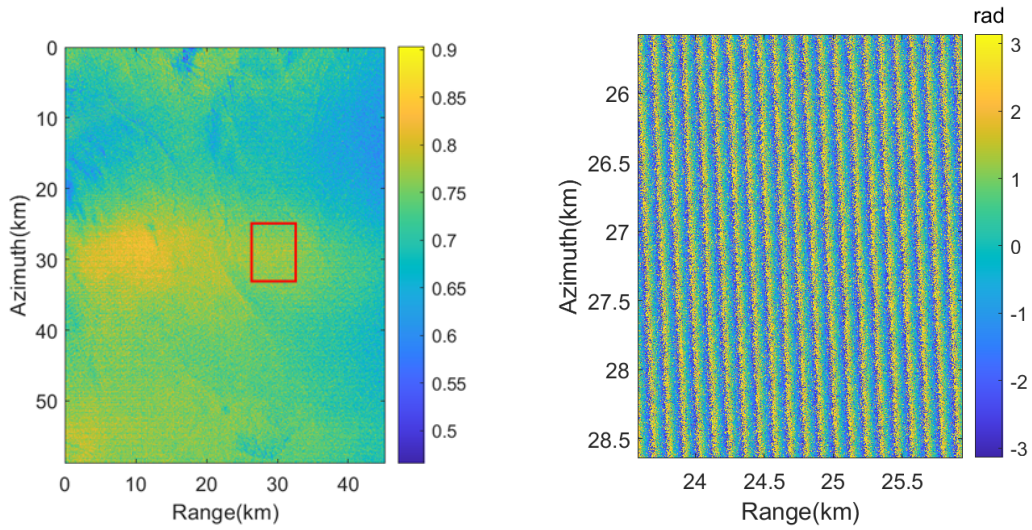

(**a**) (**b**)

Figure 7. (**a**) Correlation coefficient between primary and secondary images. (**b**) Interferometric phase diagram. The red box in the left column indicates the area corresponding to the interference fringes on the right.

4.2. Cross-Track Baseline Component Phase Removal

The LuTan-1 InSAR system operates in a unique double-helix formation during flight, resulting in temporally varying cross-track baseline components. These variations introduce flat Earth and height phase errors in ocean surface velocity measurements [36]. Before removing the cross-track phase component, a multi-looking process is applied to the interferogram to reduce the phase noise and improve phase accuracy, albeit at the expense of spatial resolution. This study employed a 64 × 64 window size for the multi-looking operation, resulting in an approximate spatial resolution of 89.6 m in the azimuth direction and 106.8 m in the range direction. To obtain accurate ocean surface velocity measurements, it is necessary to correct for the interferometric phase induced by the cross baseline. This study employed a two-step strategy. In the first step, the theoretical cross-track baseline phase was computed based on satellite navigation system positioning and external sea surface height data and then subtracted from the co-registered interferometric phase. This step is commonly referred to as the orbit-based method. However, owing to limitations in the measurement accuracy of hardware systems, the navigation data from many satellites are not sufficiently precise, as observed in various SAR systems such as RADARSAT-1 [37], RADARSAT-2 [38], JERS-1 [39], Sentinel-1 [40], ALOS [41], and Gaofen-3 [42,43]. Consequently, residual cross-baseline phases may remain, leading to inaccuracies in the subsequent inversion of sea surface currents. Given that the phase information induced by sea surface currents is typically small, achieving a high level of precision in cross-baseline phase removal is essential. In the second step, a parameterized model-based approach was proposed to mitigate these residual components further. This method is effective and easy to implement. Unlike the commonly used polynomial fitting methods [44–49], the proposed approach has a clear physical interpretation.

Figure 8 shows a schematic of the imaging geometries of the hybrid interferometric SAR systems. The xyz coordinate system originates at the position of the leading antenna A_1 at time t, with the x-axis aligned with the flight direction, the z-axis vertically oriented upward from the Earth's center to the satellite's position, and the y-axis defined by the right-hand rule. Variables B_x, B_y, and B_z denote the baseline vector components along the x, y, and z axes, respectively. R_1 and R_2 are the respective distances from antennas A_1 and A_2 to the oceanic scatterers. Further, $\triangle t$ is the time delay. In Figure 8, when antenna

pointing errors are disregarded, B_x is equal to zero, leading to a distance difference $\triangle R$ between $A_2(t+\triangle t)$ and $A_1(t)$ relative to the same oceanic target, as shown by (13).

$$\begin{aligned}\Delta R &= R_2(t+\Delta t) - R_1(t) \\ &= v_{\mathrm{r}}\Delta t - B_y \sin\theta_L + B_z \cos\theta_L\end{aligned} \tag{13}$$

where θ_L denotes the look angle. Consequently, we can obtain

$$\phi = -\frac{4\pi}{\lambda}\left(v_{\mathrm{r}}\Delta t - B_y \sin\theta_L + B_z \cos\theta_L\right). \tag{14}$$

$$v_{\mathrm{r}} = -\frac{1}{\Delta t}\left(\frac{\lambda}{4\pi}\phi - B_y \sin\theta_L + B_z \cos\theta_L\right) \tag{15}$$

where $\left(B_z \cos\theta_L - B_y \sin\theta_L\right)$ is the cross-track baseline component that contributes to distortions in the radial velocity measurements. B_y and B_z can be computed from the satellite's orbital data files. To accurately calculate θ_L, it is essential to determine the precise position vector of each pixel in the SAR image within WGS-84; the coordinate system can first be established according to (16).

$$\begin{cases} \frac{(X_P+Y_P)^2}{(a\cdot\beta)^2} + \frac{Z_P^2}{(b\cdot\beta)^2} = 1 \\ R = |\mathbf{P}-\mathbf{S}| \\ f_{\mathrm{Dop}} = 2\mathbf{V}\cdot(\mathbf{P}-\mathbf{S})/\lambda \\ \beta = 1 + h_{\mathrm{sea}}\,/R_e \end{cases} \tag{16}$$

where $\mathbf{P} = \left(x_p, y_p, z_p\right)$ is the position vector of the ground point in the WGS-84 coordinate system, a and b represent the semi-major and semi-minor axes of the Earth, respectively, R is the distance vector from the platform to the sea surface target, and S is the platform position vector at each azimuth moment. H_{sea} indicates the local elevation of the sea surface, and R_e refers to the Earth's localized radius. $\mathbf{P} = \left(x_p, y_p, z_p\right)$ in (16) can be solved using Newton's iteration method. Furthermore, θ_L can be precisely calculated in accordance with (17) and (18).

$$\cos\beta_e = \frac{R_e^2 + (R_e+h)^2 - R^2}{2R_e(R_e+h_{sea})}. \tag{17}$$

$$\sin\theta_L = \frac{R_e\cdot\sin\beta_e}{R}. \tag{18}$$

where β_e represents the local geocentric angle. The meanings of the other parameters are the same as before.

$$\varphi = \frac{2\pi B_{XT}\sin(\theta_L-\alpha)}{\lambda} + \varphi_0 = \varphi_{\mathrm{fringe}} + 2\pi\mathrm{n} \tag{19}$$

$$(B_{XT}, \hat{\alpha}, \varphi_0) = \arg\min\left[\varphi_{\mathrm{fringe}} - \varphi(B_{XT}, \alpha, \varphi_0)\right] \tag{20}$$

After determining the value of θ_L using the aforementioned steps , this value of θ_L is substituted into (14) to obtain the interference phase after initially removing the cross-track interferometric phase. Figure 9a shows the phase diagram after the initial removal using the orbit information provided by LuTan-1. Compared to Figure 7b, the frequency of the interferometric fringes is significantly reduced. However, there are still significant cross-track interferometric stripes.

Two potential sources of this error were identified. The first stems from discrepancies in the altitude, including the satellite altitude and sea surface height. It is worth emphasizing that the height error alone is insufficient to account for the observed consistently shifting stripes. The problem may instead be attributed to baseline errors, encompassing variations

in both baseline length and inclination angle. Therefore, it is recommended that refinement techniques be employed to enhance the elimination of the cross-track interferometric phase.

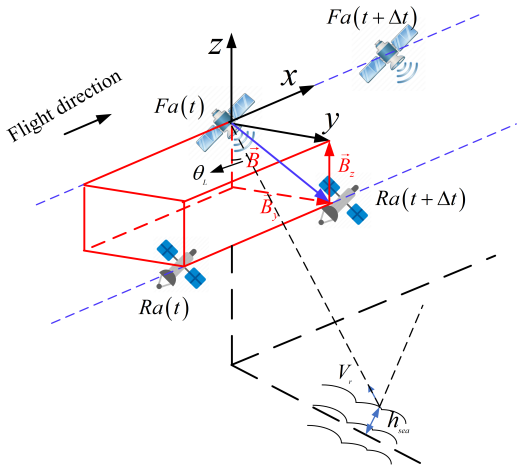

Figure 8. Acquisition geometry of hybrid interferometric SAR.

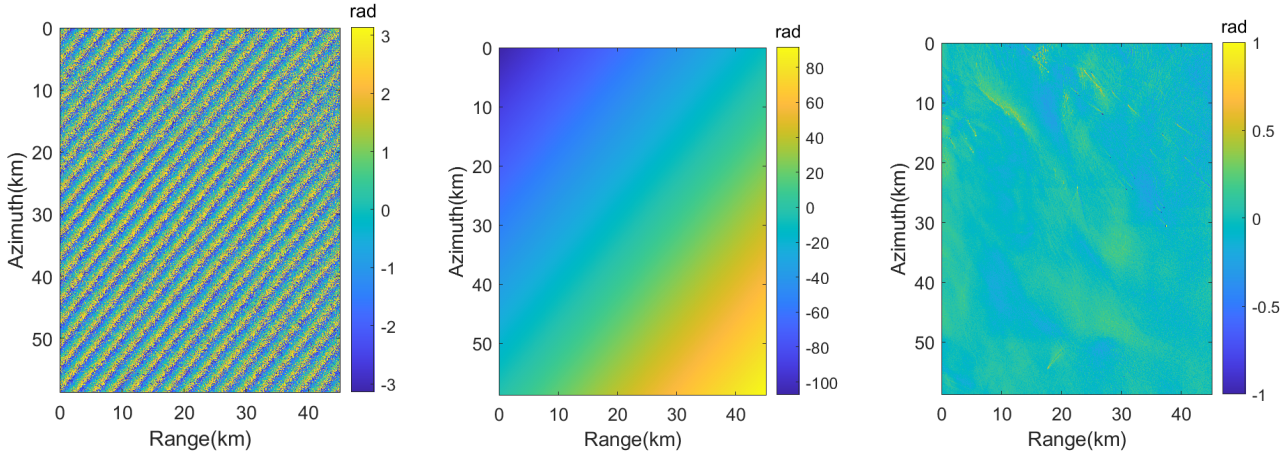

(**a**) (**b**) (**c**)

Figure 9. (**a**) The residual fringe after the orbit-based method. (**b**) The fitted flat Earth phase. (**c**) The re-flattened interferograms. The color map represents the interferometric phase.

Based on the geometric relationships, the expression for the cross-track baseline phase component is given by (19), where φ_{fringe} represents the interferometric phase fringes in the actual data. It can be regarded as the phase fringes after applying the orbit-based method, as shown in Figure 9a. The interferometric fringes in the figure contain the calibration parameter information for the LuTan-1 system. First, the phase data in Figure 9a undergo multi-looking to reduce phase noise. Since (19) describes the unwrapped phase, the phase in Figure 9a must be unwrapped. Based on the characteristics of Figure 9a, the unwrapping is performed in both the azimuth and range directions, yielding the unwrapped phase. Subsequently, the correlation coefficients from Figure 7a are used as weights for a weighted least-squares fit between the unwrapped phase and the theoretical phase described by (19). By adjusting the cross-track baseline length, tilt angle, and initial phase, the best-fit parameters are obtained when the root-mean-square error (RMSE) between the actual and fitted phases is minimized, thus satisfying the condition in (20). This process is repeated for each azimuth gate. Finally, by subtracting the fitted phase from the actual residual phase, the phase with the cross-track baseline component removed is obtained, as illustrated in Figure 9c. At this stage of processing, we obtained a fairly good-looking interferometric phase induced by the Doppler velocity.

4.3. Ocean Current Inversion

The phase of the ATI-SAR is directly proportional to the Doppler velocity of the ocean surface. After acquiring the along-track interference phase, the horizontal Doppler velocity can be derived using (4) and (5). Owing to the intricate characteristics of the ocean environment and the complicated SAR imaging mechanism for sea surfaces, the Doppler velocity obtained from the ATI phase serves as a comprehensive estimate of different velocities, as shown in (21).

$$u_{\mathrm{d}} = u_c + u_p. \tag{21}$$

where u_c denotes the sea surface current, encompassing the tidal currents and ocean currents. u_p denotes the pseudo current. In most cases, u_c is the physical quantity of concern, and the remaining components (u_p) can be regarded as interference terms. u_p is the sea surface velocity related to wind and waves. Specifically, it contains surface wind-generated currents, the orbital velocity of large-scale waves, and the net Bragg wave phase velocity, where wind-generated currents are the dominant disturbance terms. To obtain u_c, it is crucial to reduce the effect of the wind field on the Doppler velocities. While the C-band Doppler frequency (CDOP) empirical model may effectively address this issue for C-band SAR, such as ENVISAT, Gaofen-3, and Sentinel-1 [50], no equivalent empirical model is currently available for L-band spaceborne InSAR systems such as LuTan-1. The modeling system for SAR sea surface simulation (M4S) [26] was used to remove the wind-generated currents to obtain a precise sea surface current field. The M4S model is an advanced tool used for SAR imaging simulations of ocean surfaces under various scenarios. It is highly efficient in simulating the SAR interference phase of a given sea surface current and wind field.

Figure 10 is a schematic flowchart illustrating the correction inversion approach for generating the current field in ATInSAR based on the M4S model [51]. The initial step involves configuring crucial parameters for the current field correction procedure, such as the maximum number of iterations and predefined threshold values. Subsequently, the Doppler phase computed in Section 4.2, referred to as the initial-guess phase, along with wind field data, radar parameters, and platform parameters, were provided as inputs to the M4S model to calculate the initial-guess current field. Following processing by two modules, M4Sw and M4Sr, which, respectively, handle the computation of the wave spectrum and the calculation of the current field, a comparative analysis was conducted between the simulated and initial-guess current fields.

The process of determining the "optimal current field" followed specific criteria. The process terminated when the RMSE of two adjacent iterations was lower than the set threshold and gradually tended to a specific value. Otherwise, the iteration continued unless the maximum number of iterations was exceeded. The current field underwent correction for the subsequent iteration. The corrected current field can be expressed as follows:

$$u_{ij}^{n+1} = u_{ij}^{n} + \lambda \Delta u \tag{22}$$

where n denotes the n th iteration, u_{ij} denotes the velocity of the (i, j)th pixel, λ is the scaling factor, ranging from 0 to 1, and Δu signifies the speed difference between two successive iterations, where $\lambda = 0.238$ m , and the RMSE threshold is 0.015 rad. Figure 11a displays a graph of the RMSE change as the number of iterations increased. It is evident that the RMSE gradually decreased from 0.045 rad and approached 0.011 rad. Figure 11b shows a graph of the percentage of points that satisfy the convergence conditions as the number of iterations increases. The figure shows that the satisfaction rate varies from below 30% to over 95%, indicating that the retrieved current converged. Figure 12a shows the final alternative output current field obtained using the hybrid InSAR images of LuTan-1.

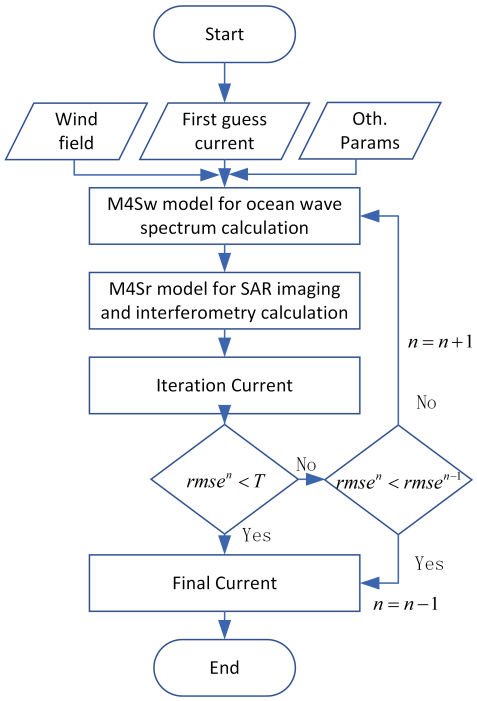

Figure 10. M4S model ATI-SAR ocean surface retrieval process.

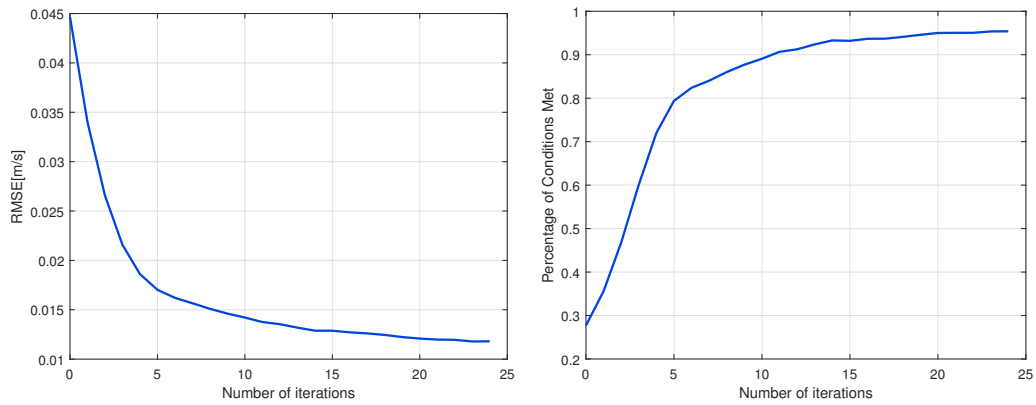

(**a**) (**b**)

Figure 11. (**a**) Variation in RMSE with number of iterations. (**b**) Percentage of points that meet convergence conditions with increasing number of iterations.

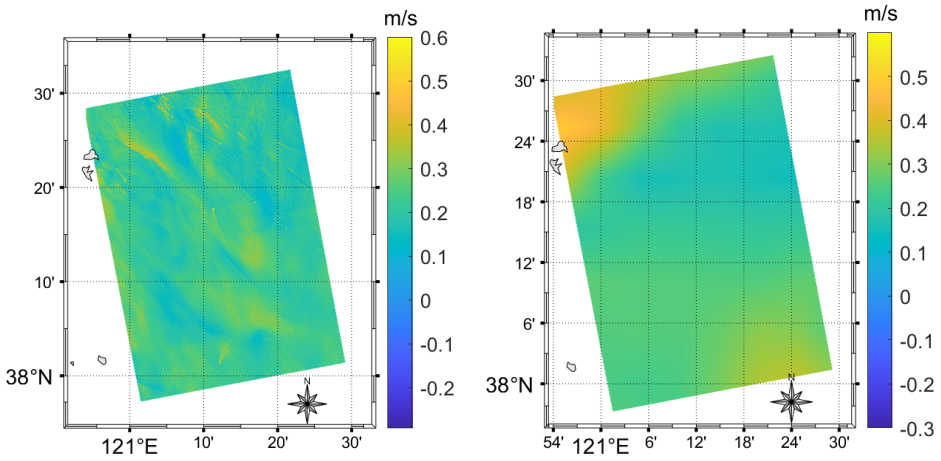

(**a**) (**b**)

Figure 12. (**a**) Sea surface velocity from LuTan-1. (**b**) Sea surface velocity reference data from CMEMS. Color map represents radial current velocity.

5. Results and Discussion

Due to the absence of in situ measurement data in the experimental region, such as those from buoys and coastal radars, two approaches were adopted to validate the accuracy and effectiveness of the inversion results. First, a quantitative comparison was conducted between the inversion results and reference data from the CMEMS. Second, a qualitative analysis of sub-mesoscale oceanic phenomena, such as ship wakes, observed in the inversion results was performed based on oceanographic characteristics.

5.1. Quantitative Validation

Figure 12b shows the current reference data from the CMEMS. The data were transformed to align with the radial direction of LuTan-1.

The CMEMS dataset provides average information regarding large-scale spatial features of the sea surface. Based on these reference values, the InSAR measurements offer significantly higher resolution and accuracy in capturing detailed sea surface characteristics. Therefore, this validation focuses on comparing the ATI-derived surface current measurements with the relative deviations from the CMEMS reference data. Owing to the significantly lower spatial resolution of CMEMS reference data (0.083° lon/lat) compared to LuTan-1, quantitative comparisons were conducted exclusively at the sampling points of CMEMS. A statistical comparison of the ATI-derived ground range direction current velocity array $\boldsymbol{a} = (a_{ij})$ and CMEMS current velocity array $\boldsymbol{b} = (b_{ij})$ was conducted, considering the mean differences as follows:

$$\mathrm{MAE} = \left\langle \sum \sum |a_{ij} - b_{ij}| \right\rangle \tag{23}$$

The root-mean-square (RMS) difference can be calculated as follows:

$$\mathrm{RMSE} = \sqrt{\left\langle \sum \sum (a_{ij} - b_{ij})^2 \right\rangle} \tag{24}$$

The correlation coefficient can be determined as follows:

$$R = \frac{\sum (a_{ij} - \bar{a})(b_{ij} - \bar{b})}{\sqrt{\sum (a_{ij} - \bar{a})^2 \sum (b_{ij} - \bar{b})^2}} \tag{25}$$

Figure 13 shows a scatter diagram illustrating the relationship between the inverse current and the CMEMS data within an identical coverage region. Notably, the CMEMS data reflect the average results within 6 hours, whereas SAR captures the transient results during imaging. Therefore, it is unrealistic to expect perfect alignment between the inversion results and CMEMS data. The mean differences between the currents derived from LuTan-1 and CMEMS were 0.033 m/s, with an RMS value of 0.041. The correlation coefficient was 0.610. The statistical comparison results demonstrated relatively good consistency between the inverse current and the CMEMS data.

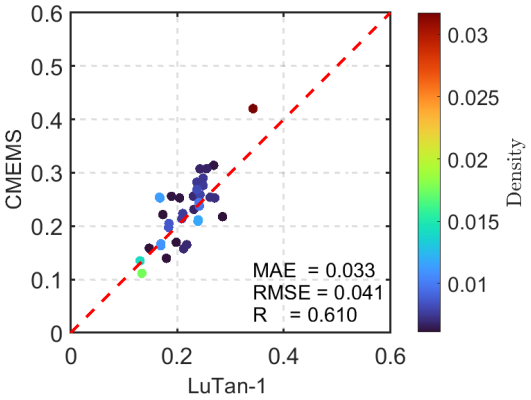

Figure 13. A scatter diagram of the LuTan-1 ATI currents versus the CMEMS reference data. The color map shows the point density per pixel. The red line represents the reference line where $y = x$.

5.2. Ship Wake Verification Analysis

ATI-SAR exhibits significant advantages in the observation of oceanic sub-mesoscale phenomena. In the inversion results (Figure 14), a multitude of wake features appear in the radial velocity distribution. This section focuses on analyzing the characteristics of ship wakes present in the ATI-derived surface current field. Although ship wakes in SAR images typically include Kelvin wakes, turbulent wakes, narrow-V wakes, and internal wave wakes [3,52], Kelvin wakes, and turbulent wakes are the most frequently observed. As shown in Figure 15a, the divergent wave arm on the ship's left side moved faster and is more prominent than that on the right side. This phenomenon can be attributed to two factors: the propagation of divergent waves from the ship as it moved and the fact that these waves traveled in a direction perpendicular to the radar line of sight. Consequently, the left-side divergent wave gradually approached the radar's line of sight, while the right-side wave moved away, causing the left-side wave to have a higher velocity and more distinct features than the right-side one.

As shown in Figure 15b, several ships are moving in opposite directions in this cropped image. Furthermore, the velocity of the left-side divergent Kelvin wave is greater than that of the right side, consistent with the conclusion we drew from Figure 15a. Additionally, the turbulent wakes of ships moving toward the scene's upper left corner exhibit higher velocities than those of ships moving toward the lower right. This is because the turbulent wakes are primarily influenced by the combined effects of the ship's jet stream and vortices generated during movement, with some whitecap foam being carried forward by the ship's motion, resulting in this phenomenon. Furthermore, the velocity of some turbulent wakes is greater than that of the Kelvin wakes (left or right divergent waves), as the propagation speed of divergent waves is typically slower than the ship's speed. However, the jet stream in the turbulent wake region moves at nearly the same speed as the ship, creating this velocity difference. From the above analysis, we can conclude that the velocity characteristics of the ship wake, as derived from the ATI current inversion results, are consistent with oceanographic and hydrodynamic principles. This consistency further validates the accuracy of the proposed ATI current inversion process and the results.

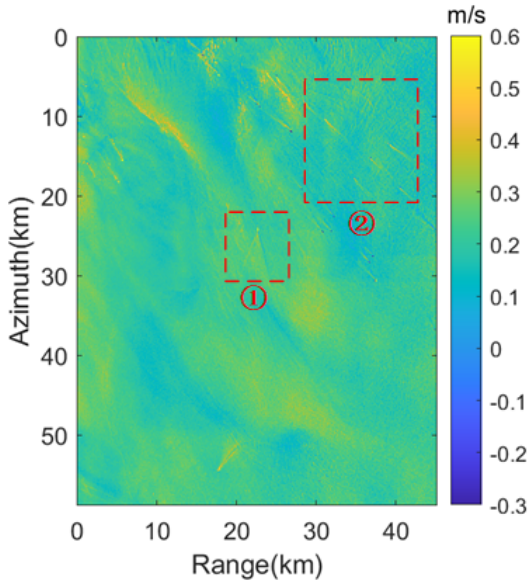

Figure 14. The sea surface velocity retrieved by ATI. The color map represents the radial current velocity.

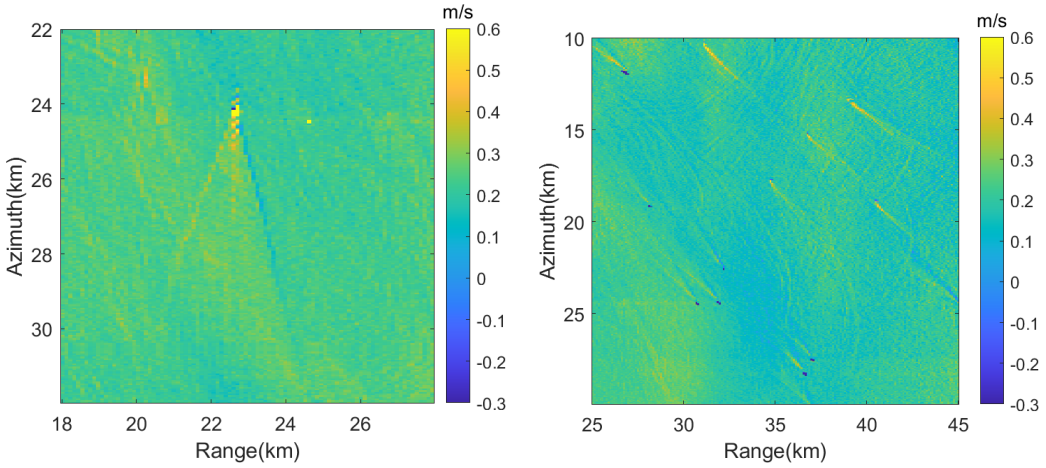

Figure 15. Enlarged views of selected subregions from Figure 14: (**a**) Region 1, (**b**) Region 2. The color map represents the radial current velocity.

6. Conclusions

Sea surface currents play a crucial role in the dynamic ocean environment. ATI-SAR technology applied to ocean current inversion yields precise measurements, a large mapping area, frequent observations, and high resolution. However, the operational implementation of interferometric SAR for ocean current inversion is challenging. One critical issue is maintaining an optimal baseline configuration for an extended duration within a satellite's orbital period. The optimal baseline length of an ATI system is approximately inversely proportional to the operating frequency. A potential approach to address this challenge is using lower frequency bands, such as the L-band, which allows for the implementation of satellite formations to achieve the optimal operational state for the ATI system. LuTan-1 is the first L-band spaceborne distributed interferometric SAR system. Although not initially designed to measure ocean currents, this instrument offers valuable guidance regarding the operational implementation of ATI-SAR on spacecraft.

On 18 July 2022, sea surface current observational data were obtained for the YanTai Sea region in China using the LuTan-1 satellite. The LuTan-1 InSAR system operates in a double-helix formation, comprising both along-track and cross-track configurations. It

operates within the optimal effective along-track baseline range of 200 to 300 m at this latitude. This study represents the first validation of ocean current measurements in L-band spaceborne ATI systems using LuTan-1. Owing to the limitations in navigation system accuracy, distributed satellite formations introduce more significant baseline errors compared to single-satellite systems. These errors make it challenging to eliminate the cross-track baseline phase component using only satellite-provided navigation parameters.

To address this issue, an easily implementable two-step strategy was proposed. The critical aspect of this approach is the use of a parameterized model for baseline error estimation, which facilitates an unambiguous physical interpretation compared to the commonly used polynomial fitting methods. To assess the precision of the inversion results, they were compared with CMEMS data. Although LuTan-1 was not specifically designed for measuring ocean currents, the quantitative comparison results were relatively consistent.

The mean differences between the currents obtained from CMEMS and LuTan-1 were 0.032 m/s and 0.041 m/s, respectively, with a correlation coefficient of 0.610. This study demonstrates the viability of measuring sea surface currents using a spaceborne L-band SAR system by processing LuTan-1 interference data. It also offers insights into the potential for the future operational deployment of a spaceborne ATI-SAR system for ocean current velocity measurements. However, several limitations need to be addressed. One notable limitation is the lack of local real-time data on wind speed, sea surface velocity, and sea surface height. Herein, the local sea surface current velocity and height data were sourced from CMEMS, whereas the sea surface wind speed data were obtained from the ECMWF. These data sources represent the average measurement over a long duration and large area. LuTan-1 acquired data within a few seconds of the synthetic aperture. They are not compatible, and this mismatch leads to errors during result verification and processing.

Author Contributions: Conceptualization, B.P. and T.L. (Tao Lai); Data Curation, B.P., X.Y. and T.L. (Tao Li); Formal Analysis, B.P. and C.X.; Funding Acquisition, X.W. and H.H.; Investigation, B.P. and T.L. (Tao Lai); Methodology, B.P., T.L. (Tao Lai), X.W. and H.H.; Project Administration, H.H.; Resources, B.P., X.Y. and X.W.; Software, B.P.; Supervision, H.H.; Validation, B.P.; Writing—Original Draft, B.P.; Writing—Review and Editing, B.P., X.W. and H.H. All authors have read and agreed to the published version of the manuscript.

Funding: This work was supported in part by the National Natural Science Foundation of China under Grant 62071499 and in part by the National Natural Science Foundation of China under Grant 62031005.

Data Availability Statement: The data presented in this study are available on request from the corresponding author.

Conflicts of Interest: The authors declare no conflicts of interest.

References

1. Zhang, Y.; Zhang, H.; Hou, S.; Deng, Y.; Yu, W.; Wang, R. An innovative superpolyhedron (SP) formation for multistatic SAR (M-SAR) interferometry. *IEEE Trans. Geosci. Remote Sens.* **2021**, *59*, 10136–10150. [CrossRef]
2. Goldstein, R.M.; Zebker, H. Interferometric radar measurement of ocean surface currents. *Nature* **1987**, *328*, 707–709. [CrossRef]
3. Xu, C.; Qi, R.; Wang, X.; Tao, M. Instability of energy spectrum disturbance for ship turbulent wakes: SAR imaging simulation and analysis. *Ocean. Eng.* **2024**, *292*, 116502. [CrossRef]
4. Elyouncha, A.; Eriksson, L.E.; Romeiser, R.; Ulander, L.M. Empirical relationship between the Doppler centroid derived from X-band spaceborne InSAR data and wind vectors. *IEEE Trans. Geosci. Remote. Sens.* **2021**, *60*, 1–20. [CrossRef]
5. Yang, Z.; Fang Zhao, C.; Miao, H. Retrieval of SEA Surface Radial Current Velocity based on Sentinel-1 Ocean Data. In Proceedings of the IGARSS 2022-2022 IEEE International Geoscience and Remote Sensing Symposium, Kuala Lumpur, Malaysia, 7–22 July 2022; IEEE: Piscataway, NJ, USA, 2022; pp. 7030–7033.
6. Romeiser, R.; Runge, H. Theoretical evaluation of several possible along-track InSAR modes of TerraSAR-X for ocean current measurements. *IEEE Trans. Geosci. Remote Sens.* **2006**, *45*, 21–35. [CrossRef]

7. Moccia, A.; Rufino, G. Spaceborne along-track SAR interferometry: Performance analysis and mission scenarios. *IEEE Trans. Aerosp. Electron. Syst.* **2001**, *37*, 199–213. [CrossRef]
8. Van Zyl, J.J. The Shuttle Radar Topography Mission (SRTM): A breakthrough in remote sensing of topography. *Acta Astronaut.* **2001**, *48*, 559–565. [CrossRef]
9. Rodriguez, E.; Morris, C.S.; Belz, J.E. A global assessment of the SRTM performance. *Photogramm. Eng. Remote Sens.* **2006**, *72*, 249–260. [CrossRef]
10. Romeiser, R.; Breit, H.; Eineder, M.; Runge, H. Demonstration of current measurements from space by along-track SAR interferometry with SRTM data. In Proceedings of the IEEE International Geoscience and Remote Sensing Symposium, Toronto, ON, Canada, 24–28 June 2002; IEEE: Piscataway, NJ, USA, 2002; Volume 1, pp. 158–160.
11. Farr, T.G.; Rosen, P.A.; Caro, E.; Crippen, R.; Duren, R.; Hensley, S.; Kobrick, M.; Paller, M.; Rodriguez, E.; Roth, L.; et al. The shuttle radar topography mission. *Rev. Geophys.* **2007**, *45*, RG2004. [CrossRef]
12. Romeiser, R.; Breit, H.; Eineder, M.; Runge, H.; Flament, P.; De Jong, K.; Vogelzang, J. Current measurements by SAR along-track interferometry from a space shuttle. *IEEE Trans. Geosci. Remote Sens.* **2005**, *43*, 2315–2324. [CrossRef]
13. Werninghaus, R.; Buckreuss, S. The TerraSAR-X mission and system design. *IEEE Trans. Geosci. Remote Sens.* **2009**, *48*, 606–614. [CrossRef]
14. Romeiser, R.; Suchandt, S.; Runge, H.; Steinbrecher, U.; Grunler, S. First analysis of TerraSAR-X along-track InSAR-derived current fields. *IEEE Trans. Geosci. Remote Sens.* **2009**, *48*, 820–829. [CrossRef]
15. Rashid, M.; Gierull, C. Gulf stream detection and estimation with RADARSAT-2 along-track interferometry. In Proceedings of the IGARSS 2020-2020 IEEE International Geoscience and Remote Sensing Symposium, Virtual, 26 September–2 October 2020; IEEE: Piscataway, NJ, USA, 2020; pp. 1–4.
16. Rashid, M.; Gierull, C.H. Retrieval of ocean surface radial velocities with RADARSAT-2 along-track interferometry. *IEEE J. Sel. Top. Appl. Earth Obs. Remote. Sens.* **2021**, *14*, 9597–9608. [CrossRef]
17. Yuan, X.; Lin, M.; Han, B.; Zhao, L.; Wang, W.; Sun, J.; Wang, W. Observing Sea Surface Current by Gaofen-3 Satellite Along-Track Interferometric SAR Experimental Mode. *IEEE J. Sel. Top. Appl. Earth Obs. Remote. Sens.* **2021**, *14*, 7762–7770. [CrossRef]
18. Krieger, G.; Moreira, A.; Fiedler, H.; Hajnsek, I.; Werner, M.; Younis, M.; Zink, M. TanDEM-X: A satellite formation for high-resolution SAR interferometry. *IEEE Trans. Geosci. Remote Sens.* **2007**, *45*, 3317–3341. [CrossRef]
19. Romeiser, R.; Runge, H. Measuring the temporal autocorrelation function of backscattered X-band signals from the ocean with TanDEM-X. In Proceedings of the EUSAR 2014, 10th European Conference on Synthetic Aperture Radar, Berlin, Germany, 3–5 June 2014; pp. 1–3.
20. Romeiser, R.; Runge, H.; Suchandt, S.; Kahle, R.; Rossi, C.; Bell, P.S. Quality assessment of surface current fields from TerraSAR-X and TanDEM-X along-track interferometry and Doppler centroid analysis. *IEEE Trans. Geosci. Remote Sens.* **2013**, *52*, 2759–2772. [CrossRef]
21. Gommenginger, C.; Chapron, B.; Marquez, J.; Richards, B.; Caparrini, M.; Burbidge, G.; Cotton, D.; Martin, A.C. Wavemill: A new mission for high-resolution mapping of total ocean surface current vectors. In Proceedings of the EUSAR 2014; 10th European Conference on Synthetic Aperture Radar, Berlin, Germany, 3–5 June 2014; pp. 1–4.
22. Gommenginger, C.; Chapron, B.; Hogg, A.; Buckingham, C.; Fox-Kemper, B.; Eriksson, L.; Soulat, F.; Ubelmann, C.; Ocampo-Torres, F.; Nardelli, B.B.; et al. SEASTAR: A mission to study ocean submesoscale dynamics and small-scale atmosphere-ocean processes in coastal, shelf and polar seas. *Front. Mar. Sci.* **2019**, *6*, 457. [CrossRef]
23. Martin, A.; Gommenginger, C.; Chapron, B.; Márquez, J.; Doody, S.; Cotton, D.; Buck, C. Dual beam along-track interferometic SAR to MAP total ocean surface current vectors with the airborne wavemill proof-of-concept instrument: Impact of wind-waves. In Proceedings of the 2015 IEEE International Geoscience and Remote Sensing Symposium (IGARSS), Milan, Italy, 6–31 July 2015; IEEE: Piscataway, NJ, USA, 2015; pp. 4069–4072.
24. Gabrielli, S.; Jonas, C.; Guerrucci, R.; Jesswein, K.; Falconi, M.T.; Perfetto, D.M.; Binci, A.; Zaccari, G.; Mapelli, D. Earth Explorer 11-SEASTAR Phase 0. In Proceedings of the EUSAR 2024; 15th European Conference on Synthetic Aperture Radar, Munich, Germany, 23–26 April 2024; pp. 1017–1021.
25. Kahle, R.; Runge, H.; Ardaens, J.S.; Suchandt, S.; Romeiser, R. Formation flying for along-track interferometric oceanography—First in-flight demonstration with TanDEM-X. *Acta Astronaut.* **2014**, *99*, 130–142. [CrossRef]
26. Romeiser, R.; Thompson, D.R. Numerical study on the along-track interferometric radar imaging mechanism of oceanic surface currents. *IEEE Trans. Geosci. Remote Sens.* **2000**, *38*, 446–458. [CrossRef]
27. Wang, R.; Liu, K.; Liu, D.; Ou, N.; Yue, H.; Chen, Y.; Yu, W.; Liang, D.; Cai, Y. LuTan-1: An innovative L-band spaceborne bistatic interferometric synthetic aperture radar mission. *IEEE Geosci. Remote Sens. Mag.* **2024**, *2*, 2–22. [CrossRef]
28. Cai, Y.; Li, J.; Yang, Q.; Liang, D.; Liu, K.; Zhang, H.; Lu, P.; Wang, R. First demonstration of RFI mitigation in the phase synchronization of LT-1 bistatic SAR. *IEEE Trans. Geosci. Remote Sensing* **2023**, *61*, 5217319. [CrossRef]
29. Stephen, J.F.; Adriano, J. Dual-beam interferometry for ocean surface current vector mapping. *IEEE Trans. Geosci. Remote. Sens.* **2001**, *39*, 401–414.

30. Copernicus Climate Change Service (C3S). ERA5: Fifth Generation of ECMWF Atmospheric Reanalyses of the Global Climate. Copernicus Climate Change Service Climate Data Store (CDS), 2024. Available online: https://cds.climate.copernicus.eu/datasets/reanalysis-era5-single-levels?tab=overview (accessed on 1 December 2024). [CrossRef]
31. Copernicus Marine Service. 2022. Copernicus Marine Service. Available online: http://marine.copernicus.eu (accessed on 18 July 2024).
32. Paul, S.; Pati, U.C. A comprehensive review on remote sensing image registration. *Int. J. Remote Sens.* **2021**, *42*, 5396–5432. [CrossRef]
33. Pallotta, L.; Giunta, G.; Clemente, C. Subpixel SAR image registration through parabolic interpolation of the 2-D cross correlation. *IEEE Trans. Geosci. Remote Sens.* **2020**, *58*, 4132–4144. [CrossRef]
34. Song, W.Q; Qu, J.; He, H. A method based on Integrating Real and Complex Correlation Function for InSAR Image Coregistration. *Acta Geod. Cartogr. Sin.* **2012**, *41*, 563–569.
35. Sun, D.; Wang, Y.; Xu, Z.; Zhang, Y.; Zhang, Y.; Meng, J.; Sun, H.; Yang, L. Ocean Wave Inversion Based on Hybrid Along-and Cross-Track Interferometry. *Remote Sens.* **2022**, *14*, 2793. [CrossRef]
36. Elyouncha, A.; Eriksson, L.E.; Romeiser, R.; Ulander, L.M. Measurements of sea surface currents in the Baltic Sea region using spaceborne along-track InSAR. *IEEE Trans. Geosci. Remote Sens.* **2019**, *57*, 8584–8599. [CrossRef]
37. Thompson, A.A. Overview of the RADARSAT constellation mission. *Can. J. Remote Sens.* **2015**, *41*, 401–407. [CrossRef]
38. Parihar, N.; Nathawat, M.; Das, A.; Mohan, S. Accuracy assessment of DEMs derived from multi-frequency SAR images. In Proceedings of the 2011 3rd International Asia-Pacific Conference on Synthetic Aperture Radar (APSAR), Seoul, Republic of Korea, 26–30 September 2011; IEEE: Piscataway, NJ, USA, 2011; pp. 1–4.
39. Kim, S.W.; Wdowinski, S.; Dixon, T.H.; Amelung, F.; Won, J.S.; Kim, J.W. InSAR-based mapping of surface subsidence in Mokpo City, Korea, using JERS-1 and ENVISAT SAR data. *Earth Planets Space* **2008**, *60*, 453–461. [CrossRef]
40. Sataer, G.; Sultan, M.; Emil, M.K.; Yellich, J.A.; Palaseanu-Lovejoy, M.; Becker, R.; Gebremichael, E.; Abdelmohsen, K. Remote sensing application for landslide detection, monitoring along Eastern Lake Michigan (Miami Park, MI). *Remote Sens.* **2022**, *14*, 3474. [CrossRef]
41. Nakamura, R.; Nakamura, S.; Kudo, N.; Katagiri, S. Precise orbit determination for ALOS. In Proceedings of the 20th International Symposium on Space Flight Dynamics, Annapolis, MD, USA, 24–28 September 2007.
42. Wang, J.; Yu, W.; Deng, Y.; Wang, R.; Wang, Y.; Zhang, H.; Zheng, M. Demonstration of time-series InSAR processing in Beijing using a small stack of Gaofen-3 differential interferograms. *J. Sens.* **2019**, *2019*, 4204580. [CrossRef]
43. Yang, Q.; Wang, J.; Wang, Y.; Lu, P.; Jia, H.; Wu, Z.; Li, L.; Zan, Y.; Wang, R. Image-based baseline correction method for spaceborne InSAR with external DEM. *IEEE Trans. Geosci. Remote Sens.* **2023**, *61*, 1–16. [CrossRef]
44. Massonnet, D.; Feigl, K.L. Radar interferometry and its application to changes in the Earth's surface. *Rev. Geophys.* **1998**, *36*, 441–500. [CrossRef]
45. Shirzaei, M.; Walter, T.R. Estimating the effect of satellite orbital error using wavelet-based robust regression applied to InSAR deformation data. *IEEE Trans. Geosci. Remote Sens.* **2011**, *49*, 4600–4605. [CrossRef]
46. Liu, Z.; Jung, H.S.; Lu, Z. Joint correction of ionosphere noise and orbital error in L-band SAR interferometry of interseismic deformation in southern California. *IEEE Trans. Geosci. Remote Sensing* **2013**, *52*, 3421–3427. [CrossRef]
47. Suchandt, S.; Runge, H. Ocean surface observations using the TanDEM-X satellite formation. *IEEE J. Sel. Top. Appl. Earth Obs. Remote Sens.* **2015**, *8*, 5096–5105. [CrossRef]
48. Elyouncha, A.; Eriksson, L.E.; Romeiser, R.; Ulander, L.M. Phase calibration of TanDEM-X ATI-SAR data for sea surface velocity measurements. In Proceedings of the 2017 IEEE International Geoscience and Remote Sensing Symposium (IGARSS), Fort Worth, TX, USA, 23–28 July 2017; IEEE: Piscataway, NJ, USA, 2017; pp. 922–925.
49. Du, Y.; Fu, H.; Liu, L.; Feng, G.; Peng, X.; Wen, D. Orbit error removal in InSAR/MTInSAR with a patch-based polynomial model. *Int. J. Appl. Earth Obs. Geoinf.* **2021**, *102*, 102438. [CrossRef]
50. Miao, Y.; Dong, X.; Bourassa, M.A.; Zhu, D. Effects of ocean wave directional spectra on Doppler retrievals of ocean surface current. *IEEE Trans. Geosci. Remote Sens.* **2021**, *60*, 1–12. [CrossRef]
51. Yu, X.Z.; Chong, J.S.; Hong, W. An Iterative Method for Ocean Surface Current Retrieval by Along-track Interferometric SAR. *J. Electron. Inf. Technol.* **2012**, *34*, 2660–2665. [CrossRef]
52. Xu, C.; Wang, Q.; Wang, X.; Chao, X.; Pan, B. Wake2Wake: Feature-Guided Self-Supervised Wave Suppression Method for SAR Ship Wake Detection. *IEEE Trans. Geosci. Remote Sens.* **2024**, *62*, 5108114. [CrossRef]